# A Stochastic Interacting Particle-Field Algorithm for a Haptotaxis Advection-Diffusion System Modeling Cancer Cell Invasion

Boyi Hu* Zhongjian Wang † Jack Xin ‡ Zhiwen Zhang§

August 18, 2024

**Abstract**

The study of tumor invasion and metastasis dynamics is of utmost importance for the advancement of cancer biology and treatment. Many mathematical models have been developed to investigate the process of host tissue invasion by tumor cells. In this paper, we develop a novel stochastic interacting particle-field (SIPF) algorithm that accurately simulates the cancer cell invasion process within the haptotaxis advection-diffusion (HAD) system. Our SIPF algorithm approximates the cell density by empirical measures of particles and approximates the coupled smooth fields, which are the extracellular matrix concentration (ECM) and matrix-degrading enzymes (MDEs) by the spectral method. We derive a one-step time recursion for both the positions of stochastic particles and the field variables using the implicit Euler discretization, which is based on the explicit Green's function of an elliptic operator characterized by the Laplacian minus a positive constant. Finally, we conduct numerical experiments to demonstrate the superior performance of the proposed algorithm, especially in computing cancer cell growth with thin free boundaries in three-dimensional (3D) space. Numerical results show that the SIPF algorithm is mesh-free, self-adaptive, and low-cost. Moreover, it is more accurate and efficient than traditional numerical techniques such as the finite difference method (FDM) and spectral methods.

**Keywords** Mathematical models, haptotaxis advection-diffusion (HAD) system, interacting particle-field approximation, cancer cell invasion process, three-dimensional (3D) simulations.

*Department of Mathematics, The University of Hong Kong, Pokfulam Road, Hong Kong SAR, P.R.China. huby22@connect.hku.hk.

†Division of Mathematical Sciences, School of Physical and Mathematical Sciences, Nanyang Technological University, 21 Nanyang Link, Singapore 637371. zhongjian.wang@ntu.edu.sg

‡Department of Mathematics, University of California at Irvine, Irvine, CA 92697, USA. jack.xin@uci.edu

§Corresponding author. Department of Mathematics, The University of Hong Kong, Pokfulam Road, Hong Kong SAR, P.R.China. Materials Innovation Institute for Life Sciences and Energy (MILES), HKU-SIRI, Shenzhen, P.R. China. zhangzw@hku.hk.

# 1 Introduction

The prevalence of cancer has seen a significant global increase, making it the second leading cause of death following cardiovascular diseases [19]. The study of tumor invasion and metastasis dynamics is a crucial area of research within cancer biology and treatment. Since the 1970s, various mathematical models have been developed to analyze the different phases of solid tumor growth, both in temporal and spatio-temporal contexts [4]. A significant amount of empirical data on the growth dynamics of avascular tumors has been integrated into mathematical models that utilize various growth laws, including Gompertzian, logistic, and exponential growth [18]. Additionally, stochastic growth models have been utilized to simulate the invasion of tumor cells, providing insights into the functional implications of histological patterns [20].

Mathematical modeling is a powerful tool for unraveling the complexities of biological processes, providing valuable insights that inform both experimental and clinical strategies. The field of cancer modeling has benefited from various approaches, ranging from mechanistic models that explore the detailed mechanisms of diseases to data-driven models that facilitate clinical decision-making [3]. Specifically, in the area of tumor-induced angiogenesis, researchers have developed both continuous and discrete mathematical models to simulate the formation of capillary networks triggered by tumor angiogenic factors. These models effectively integrate critical interactions between endothelial cells and the extracellular matrix concentration (ECM) [1]. Cancer cell invasion of tissue is a complex process that involves cell migration through the ECM, facilitated by the secretion of degradative enzymes [17]. This invasion is modeled using a system of partial differential equations (PDEs) that capture the dynamics involving tumor cells, the ECM, and matrix-degrading enzymes (MDEs), highlighting the intricate biological interactions essential for tissue invasion [2].

Additionally, fractional mathematical models have been introduced to better understand the complex dynamics among tumor cells, matrix degradation, and enzyme production, employing sophisticated analytical techniques such as the $q$-homotopy analysis transform method [25]. Stochastic differential equation (SDE) models have also been formulated to capture the stochastic behaviors of cancer cell migration and invasion, addressing the variability in diffusion processes within the context of PDE [10]. Furthermore, the global behavior of solutions to models of tumor invasion, which emphasize the critical role of ECM concentration, has undergone thorough analysis, providing a detailed understanding of the invasion process and its interactions with various biological factors [24, 15, 11]. The integration of these models forms a comprehensive framework of mathematical and computational approaches that significantly enhance our understanding of cancer cell invasion and metastasis. This collective body of work lays a solid foundation for the innovation of therapeutic strategies aimed at combating cancer effectively.

The Lagrangian perspective has shown substantial theoretical progress in models similar to cancer invasion, making it compelling to consider applying this framework to numerically solve problems related to cancer invasion. A convergent particle method was derived for fully parabolic chemotaxis equations [22]. The study [21] utilized cellular

automaton simulations based on a reinforced self-attracting random walk for a single particle in 1D. Building on this framework, [23] expanded the scope to derive more general chemotaxis systems from similar reinforced random walks, and further analyzed the qualitative behavior of these systems, providing deeper insights into the dynamics and implications of such models in higher dimensions and more complex scenarios. A random particle blob method has been shown to converge for the parabolic-elliptic Keller-Segel (KS) system when the macroscopic mean-field equation allows for a global weak solution [13, 12]. The success of this method largely depends on an in-depth understanding of the nonlinear mean-field equation, rather than the complexities of the multi-particle Markov process involved [16]. A deep-learning study of chemotaxis and aggregation in 3D laminar and chaotic flows has been done in [27] with a kernel regularization technique for particle dynamics.

In this paper, we propose a novel SIPF algorithm to compute the cancer cell invasion process for the haptotaxis HAD system. Our method considers the coupled stochastic particle and field evolutions, where the corresponding fields represent the ECM and MDE concentration within the system. This approach enables self-adaptive simulations that effectively handle potential singularities or free boundaries. In our SIPF algorithm, we model the density of active particles using empirical particle representation, which involves a summation of delta functions centered at the particle positions. Furthermore, we discretize the ECM and MDE, using the spectral method instead of FDM, as suggested by [6]. This choice is motivated by the fact that the fields of ECM and MDE tend to be smoother than the density. Specifically, the MDE concentration is updated through an explicit Euler scheme applied to its Fourier coefficients, leveraging the convolution theorem.

To validate the efficacy of our method, we conduct numerical experiments in 3D space. It is worth mentioning that pseudo-spectral methods have been successfully employed to compute nearly singular solutions of the 3D Euler equations [8]. In addition, the adaptive moving mesh method has been developed to investigate finite-time blowup in the 3D axisymmetric Euler equations [14]. These approaches are high-resolution methods for resolving nearly singular phenomena in the 3D Euler equations. However, it is important to acknowledge that implementing pseudo-spectral methods for 3D problems requires significant computational resources, and the adaptive moving mesh method requires intricate design and advanced coding capabilities.

In contrast, the SIPF algorithm is a simple-to-program, efficient, and low-cost method for 3D computations. We demonstrate the effectiveness of the SIPF algorithm for simulating the haptotaxis HAD system that models cancer cell invasion. The SIPF algorithm operates recursively without relying on historical data and computes the field variable (concentration) using the Fast Fourier Transforms (FFT) method. The concentration field variables are smoother than the particle density, allowing FFT to work efficiently with only a few dozen Fourier modes. We accurately capture the spreading phenomenon of the particle density using 10,000 particles. Traditional FDM is not only time-consuming but also suffers from poor precision in 3D numerical simulations. This results in an inaccurate representation of tumor invasion, as demonstrated in Fig.2 and Fig.4. These results show that our approach outperforms FDM in terms

of both computational runtime and accuracy, especially when the diffusion coefficient of cancer cell density is small. Moreover, the SIPF algorithm has a notable strength in its ability to simulate complex multi-modal cell development, such as multiple cancer cell spreading and merging dynamics, where the system has non-radial solutions; see Fig.5. This allows us to simulate complex behavior and gain valuable insights into the dynamics.

The rest of the paper is organized as follows. In Section 2, we provide a concise overview of the cancer cell invasion HAD system, including a discussion of related theoretical analyses. We introduce our SIPF algorithms, which streamline a theoretically equivalent yet computationally intensive method (involving history-dependent parabolic kernel functions) into practical recursive computations. In Section 3, we present numerical results to illustrate the efficacy of the SIPF algorithm within 3D cancer cell invasion models. Finally, we conclude with Section 4, where we summarize our results and discuss potential avenues for future research.

## 2 Cancer Cell Invasion HAD System

Consider the following cancer cell invasion HAD System (see Eq.(5) in [2]), which describes the interactions among tumor cells, ECM, and MDEs:

$$\begin{cases} \rho_t = d_n \Delta \rho - \gamma \nabla \cdot (\rho \nabla f), \\ f_t = -\eta m f, \\ m_t = d_m \Delta m - \beta m + \alpha \rho. \end{cases} \tag{1}$$

The system (1) is defined with physical and biological parameters $(d_n, \gamma, \eta, d_m, \alpha, \beta) > 0$ on a compact subset $\Omega$ of $\mathbb{R}^d$ (where $d = 2, 3$), and zero flux boundary conditions (refer to Eq.(6)-(7) in [2], with $\partial_n$ representing the outward normal derivative):

$$d_n \partial_n \rho - \gamma \rho \partial_n f = 0, \quad \partial_n m = 0; \quad \text{on } \partial\Omega. \tag{2}$$

Given that $f = f_0 \exp\left(-\eta \int_0^t m(x;\tau)\, d\tau\right)$, we have $\partial_n f = 0$ on $\Omega$ if $(\partial_n f_0, \partial_n m) = 0$ on $\partial\Omega$. Hence, the boundary conditions in (2) are replaced by the following zero Neumann boundary conditions:

$$\partial_n(\rho, m) = 0, \quad \forall t \geq 0 \text{ on } \partial\Omega; \quad \partial_n f_0 = 0 \text{ on } \partial\Omega. \tag{3}$$

The variables $\rho$, $m$, and $f$ in the system (1) are functions of both the spatial variable $x$ and time $t$. The first equation in (1) governs tumor cell motion, with $\rho$ representing the tumor cell density. Our model specifically focuses on the interactions between cells and the ECM, examining their impact on tumor cell migration without incorporating cell proliferation [9]. We choose $d_n$ to be a constant, representing the tumor cell random motility coefficient, rather than a function of either the MDE or ECM concentration.

The second equation in (1) models this degradation process of the ECM, with $f$ representing the ECM density and $\delta$ being a positive constant. We assume that the MDEs degrade the ECM when they come into contact with it. The tumor cells generate

or activate the MDEs, which then diffuse throughout the surrounding tissue. These active MDEs subsequently undergo some form of decay, either passively or actively.

The third equation in (1) describes the evolution of the MDE concentration, with $m$ representing the MDE concentration and the positive constant $d_m$ representing the MDE diffusion coefficient. For the sake of simplicity, we assume a direct and proportional relationship between the density of tumor cells and the amount of active MDEs present in the surrounding tissue. This linear association is assumed to hold regardless of the quantity of enzyme precursors secreted or the existence of endogenous inhibitors. Therefore, we initially use $\alpha\rho$ to represent the MDE production by the tumor cells and $\beta m$ to signify natural decay, respectively.

## 2.1 Global Well-Possedness of Nonnegative Solutions

The paper [11] presents theoretical analyses for the general reaction-advection-diffusion model, which has also been discussed in [15] and [7]. Here, we follow the line of proof outlined in [11]. Specifically, we set $\alpha_2 = 0$, $g(v) \equiv 1$, and $\chi(v) \equiv 1$ to simplify the system in [11] to the same as the system (1). We then proceed to nondimensionalize the system (1), resulting in the following equation system:

$$\begin{cases} \rho_t = \Delta\rho - \nabla \cdot (\rho \nabla f), \\ f_t = -mf, \\ m_t = d\Delta m - \lambda m + \rho, \\ \partial_n \rho - \rho \partial_n f = \partial_n m = 0, \qquad x \in \partial\Omega, \end{cases} \tag{4}$$

where $d = \frac{d_m}{d_n}$ and $\lambda = \frac{\beta}{\alpha}$.

We define the positive self-adjoint operator $A$ as follows:

$$A := -a\Delta + b$$

where the domain $D(A)$ is given by:

$$D(A) := \{\rho \in W^{2,p}(\Omega) : \frac{\partial \rho}{\partial n} = 0 \text{ on } \partial\Omega\}$$

Here, $p \in (1, +\infty)$, and $a$ and $b$ are both positive constants.

For $0 \leq \theta \leq 1$, the fractional powers of the operator $A$, denoted as $A^\theta$, map the space $X_p^\theta$ to $L^p(\Omega)$. The space $X_p^\theta$ is equipped with the graph norm given by:

$$\|u\|_{X_p^\theta} = \|A^\theta u\|_{L^p(\Omega)}.$$

With these notations in place, we can now state the main results on the well-posedness of the system 4 as follows:

**Proposition 1** (Theorem 3.3, [11]). *Let $\Omega \subset \mathbb{R}^N$, where $N \geq 1$, be a domain with $C^2$ boundary and let $p > N$. Suppose we are given a non-negative initial value $(\rho_0, f_0, m_0) \in W^{1,p}(\Omega) \times W^{1,\infty}(\Omega) \times X_p^\theta$, where $\theta \in \left(\frac{N+p}{2p}, 1\right)$. Then, there exists $T > 0$ (depending*

*only on* $\|\rho_0\|_{W^{1,p}(\Omega)}$, $\|f_0\|_{W^{1,\infty}(\Omega)}$, *and* $\|m_0\|_{X_p^\theta}$*) such that the system* (4) *has a unique non-negative solution* $(\rho, f, m)$ *defined on an interval* $[0,T) \subset \mathbb{R}$ *and*

$$\begin{aligned}
\rho &\in C\left([0,T); W^{1,q}(\Omega)\right) \cap C\left((0,T); W^{1,\infty}(\Omega)\right) \cap C^1\left((0,T); W^{1,q}(\Omega)\right), \\
f &\in C\left([0,T); W^{1,\infty}(\Omega)\right) \cap C^1\left((0,T); W^{1,\infty}(\Omega)\right), \\
m &\in C\left([0,T); X_p^\theta\right) \cap C\left((0,T); W^{2,p}(\Omega)\right) \cap C^1\left((0,T); X_p^\theta\right).
\end{aligned}$$

*Moreover, the solution depends continuously on the initial data.*

Proposition 1 implies the local existence, uniqueness, and non-negativity of the solution to the non-dimensionalized cancer system (4) when the initial values $(\rho_0, f_0, m_0)$ are non-negative. Based on the lemmas and propositions in Section 4 of [11], we can derive the following proposition, which shows the global existence of the solution in $\Omega \subset \mathbb{R}^3$.

**Proposition 2.** *Let* $\Omega \subset \mathbb{R}^3$ *be a domain with a smooth boundary. Given the non-negative initial value* $(\rho_0, f_0, m_0) \in L^\infty(\Omega) \times W^{1,\infty}(\Omega) \times X_p^\theta(\Omega)$*, where* $p > 3$*,* $\theta \in \left(\frac{3+p}{2p}, 1\right)$*, for all* $t \in [0,T)$*, there exists a constant* $C_p$ *that is independent of time, such that the solution* $(\rho, f, m)$ *to the system* (4) *satisfies*

$$\|\rho(\cdot,t)\|_{L^\infty(\Omega)} + \|f(\cdot,t)\|_{L^p(\Omega)} + \|m(\cdot,t)\|_{X_p^\theta(\Omega)} \le C_p.$$

*Since the solution* $(\rho, f, m)$ *is uniformly bounded in* $L^\infty(\Omega)$ *for all* $t \in [0,T)$*, the local solution can be extended to a global solution.*

## 2.2 Integral Identities

Integrating the equation for MDE concentration (the second equation in the system (1)) over the spatial domain, we can obtain that

$$\int_\Omega \Delta m \, dx = \int_{\partial\Omega} \nabla m \cdot \mathbf{n} \, dS = 0, \quad \text{due to} \quad \nabla m \cdot \mathbf{n} = 0 \quad \text{on} \quad \partial\Omega, \tag{5}$$

$$\frac{d}{dt}\int_\Omega m \, dx = -\beta \int_\Omega m \, dx + \alpha \int_\Omega \rho \, dx, \tag{6}$$

where we have used the conservation form of the equation for $\rho$ to deduce that $\int_\Omega \rho \, dx$ is conserved in time. As a result, the integral $\int_\Omega m \, dx$ can be evaluated in closed analytic form based on its initial value. Furthermore, the evolution of $f$ can be expressed in terms of $m$ as follows:

$$f = f_0 \exp\left(-\eta \int_0^t m(x;\tau) d\tau\right), \tag{7}$$

where $f_0$ denotes the initial value of $f$ at $t = 0$.

Taking the logarithm of equation (7) and integrating it over the spatial domain, we obtain:

$$\int_\Omega \ln f \, dx = \int_\Omega \ln f_0 \, dx - \eta \int_\Omega \int_0^t m(x;\tau) d\tau dx. \tag{8}$$

Since the system (4) is well-posed, $m(x;\tau)$ is integrable in $x$ and $\tau$, and the integral of $m(x;\tau)$ over $\Omega \times [0,t]$ is finite. By applying Fubini's theorem, we can interchange the order of integration, which yields:

$$\int_\Omega \ln f \, dx = \int_\Omega \ln f_0 \, dx - \eta \int_0^t \int_\Omega m(x;\tau) \, dx \, d\tau. \tag{9}$$

Thus, $\int_\Omega \ln f \, dx$ can also be evaluated in a closed analytical form via time integration of $\int_\Omega m \, dx$. These identities will be used to validate numerical approximations in Section 3.4 through equation (44).

## 2.3 SIPF Algorithm for Cancer Cell Invasion HAD System

To solve the model of invasion of host tissue by tumor cells, we utilize the SIPF algorithm, which was first developed in [28] for solving the parabolic-parabolic KS systems. We partition the time interval $[0,T]$ into temporal grid points $\{t_n\}_{n=0:n_T}$ with $t_0 = 0$ and $t_{n_T} = T$, and approximate the density $\rho$ using particles as follows:

$$\rho_t \approx \frac{M_0}{P} \sum_{j=1}^{P} \delta(\mathbf{x} - X_t^P), \quad P \gg 1, \tag{10}$$

where $M_0$ is the conserved total mass (the integral of $\rho$), and $P$ is the number of particles.

We restrict the domain $\Omega$ to $[0, L\pi]^d$ due to our utilization of the Fourier transform. For the MDE concentration $m$, we use the spectral method to approximate it. Specifically, we approximate $m(\mathbf{x},t)$ by a Fourier series:

$$\sum_{j,m,l \in \mathcal{H}} \alpha_{t;j,m,l} \exp(i2\pi j x_1/L) \exp(i2\pi m x_1/L) \exp(i2\pi l x_1/L) \tag{11}$$

where $\mathcal{H}$ denotes the index set

$$\{(j,m,l) \in \mathbb{N}^3 : |j|, |m|, |l| \le \frac{H}{2}\}, \tag{12}$$

and $i = \sqrt{-1}$.

At time $t_0 = 0$, we generate $P$ empirical samples $\{X_0^p\}_{p=1}^P$ according to the initial condition of $\rho_0$, and set up $\alpha_{0;j,m,l}$ using the Fourier series of $m_0$.

For the sake of simplicity in presenting our algorithm, we use the notations

$$\rho_n = \frac{M_0}{P} \sum_{p=1}^{P} \delta(\mathbf{x} - X_n^p) \tag{13}$$

$$m_n = \sum_{j,m,l \in \mathcal{H}} \alpha_{n;j,m,l} \exp(i2\pi j x_1/L) \exp(i2\pi m x_2/L) \exp(i2\pi l x_3/L) \tag{14}$$

$$f_n = \sum_{j,m,l \in \mathcal{H}} \beta_{n;j,m,l} \exp(i2\pi j x_1/L) \exp(i2\pi m x_2/L) \exp(i2\pi l x_3/L) \tag{15}$$

to represent the tumor cell density $\rho$, MDE concentration $m$, and ECM density $f$ at time $t_n$, respectively.

Given that $\rho_n$, $f_{n-1}$, and $m_{n-1}$ are known, inspired by the operator splitting technique, our algorithm for time stepping system (1) from $t_n$ to $t_{n+1}$ consists of three sub-steps: updating the MDE concentration $m$, updating the ECM density $f$, and updating the tumor cell density $\rho$.

*Updating MDE concentration m.* Let $\delta t = t_{n+1} - t_n > 0$ be the time step. We discretize the $m$ equation of (1) in time by an implicit Euler scheme:

$$\frac{m_n - m_{n-1}}{\delta t} = d_m \cdot \Delta m_n - \beta m_n + \alpha \rho_n. \tag{16}$$

From (16), we obtain an explicit formula for $m_n$ as follows:

$$(\Delta - \frac{\beta}{d_m} - \frac{1}{d_m \cdot \delta t}) \cdot m_n = -(\frac{1}{d_m \cdot \delta t} \cdot m_{n-1} + \frac{\alpha}{d_m} \cdot \rho_n). \tag{17}$$

It follows that:

$$m_n = m(\mathbf{x}, t_n) = -\mathcal{K}_{\delta t} * (\frac{m_{n-1}}{d_m \cdot \delta t} + \frac{\alpha}{d_m} \cdot \rho_n) = -\mathcal{K}_{\delta t} * \big(\frac{m(\mathbf{x}, t_{n-1})}{d_m \cdot \delta t} + \frac{\alpha}{d_m} \cdot \rho(\mathbf{x}, t_n)\big), \tag{18}$$

where $*$ denotes the spatial convolution operator, and $\mathcal{K}_{\delta t}$ represents the Green's function of the operator $(\Delta - \frac{1}{d_m \cdot \delta t})$.

Using the expression for $m_n$ in (18), we can compute the gradient of $m$ at time $t_n$:

$$\begin{aligned} \nabla_{\mathbf{x}} m_n = \nabla_{\mathbf{x}} m(\mathbf{x}, t_n) &= -\nabla_{\mathbf{x}} \mathcal{K}_{\delta t} * (\frac{m_{n-1}}{d_m \cdot \delta t} + \frac{\alpha}{d_m} \cdot \rho_n) \\ &= -\nabla_{\mathbf{x}} \mathcal{K}_{\delta t} * (\frac{m(\mathbf{x}, t_{n-1})}{d_m \cdot \delta t} + \frac{\alpha}{d_m} \cdot \rho(\mathbf{x}, t_n)). \end{aligned} \tag{19}$$

In $\mathbb{R}^3$, the Green's function $\mathcal{K}_{\delta t}$ is defined as:

$$\mathcal{K}_{\delta t} = \mathcal{K}_{\delta t}(\mathbf{x}) = -\frac{e^{-|\zeta|\mathbf{x}}}{4\pi|\mathbf{x}|}, \tag{20}$$

where the constant $\zeta$ satisfies $\zeta^2 = \frac{\beta}{d_m} + \frac{1}{d_m \cdot \delta t}$. We can easily find that the Green's function given in (20) has a closed-form Fourier transform,

$$\mathcal{F}\mathcal{K}_{\delta t}(\omega) = -\frac{1}{|\omega|^2 + \zeta^2}. \tag{21}$$

In Eq.(18), the term $-\mathcal{K}_{\delta t} * m_{n-1}$ can be computed using (21). This is equivalent to modifying the Fourier coefficients $\alpha_{n;j,m,l}$ as follows:

$$\frac{\alpha_{n;j,m,l}}{4\pi^2 j^2/L^2 + 4\pi^2 m^2/L^2 + 4\pi^2 l^2/L^2 + \zeta^2}.$$

To compute the second term $\mathcal{K}_{\delta t} * \rho$ in (18), we first approximate $\mathcal{K}_{\delta t}$ using a cosine series expansion. Then, using the particle representation of $\rho$ given in (10), we obtain:

$$(\mathcal{K}_{\delta t} * \rho)_{j,m,l} \approx \frac{M_0}{P} \sum_{p=1}^{P} \frac{\exp\left(-2\pi j X^p_{n,1}/L - 2\pi m X^p_{n,2}/L - 2\pi l X^p_{n,3}/L\right) (-1)^{j+m+l}}{(4\pi^2 j^2/L^2 + 4\pi^2 m^2/L^2 + 4\pi^2 l^2/L^2 + \zeta^2)}.$$

Finally, we summarize the one-step update of Fourier coefficients of the MDE concentration $m$ in Algorithm 1.

**Algorithm 1** One step update of MDE concentration in SIPF

**Require:** Distribution $\rho_n$ represented by empirical samples $X_n$, initial MDE concentration $m_{n-1}$ represented by Fourier coefficients $\alpha_{n-1}$

**for all** $(j,m,l) \in \mathcal{H}$ **do**
  $\alpha_{n;j,m,l} \leftarrow \frac{\alpha_{n-1;j,m,l}}{d_m \cdot \delta t(4\pi^2 j^2/L^2+4\pi^2 m^2/L^2+4\pi^2 l^2/L^2+\zeta^2)}$
  $F_{j,m,l} \leftarrow 0$
  **for** $p = 1$ to $P$ **do**
    $F_{j,m,l} \leftarrow F_{j,m,l} + \exp\left(-2\pi j X^p_{n;1}/L - 2\pi m X^p_{n;2}/L - 2\pi l X^p_{n;3}/L\right)$
  **end for**
  $F_{j,m,l} \leftarrow F_{j,m,l} \frac{(-1)^{j+m+l}}{4\pi^2 j^2/L^2+4\pi^2 m^2/L^2+4\pi^2 l^2/L^2+\beta^2} * \frac{M}{P}$
**end for**
$\alpha_n \leftarrow \alpha_n - \frac{\alpha}{d_m} \cdot F$

**Ensure:** Update MDE concentration field from input $m_{n-1}$ to $m_n$ via $\alpha_n$.

*Updating the ECM density $f$.* $f(\mathbf{x},t)$ has a series representation as follows:

$$\sum_{j,m,l\in\mathcal{H}} \beta_{t;j,m,l} \exp(i2\pi j x_1/L) \exp(i2\pi m x_2/L) \exp(i2\pi l x_3/L). \tag{22}$$

We discretize the $f$ equation of (1) in time by an explicit Euler scheme:

$$f(\mathbf{x},t_{n+1}) = f(\mathbf{x},t_n) - \eta \cdot m(\mathbf{x},t_n) f(\mathbf{x},t_n)\delta t. \tag{23}$$

For $f(\mathbf{x},t_{n+1})$, according to the convolution theorem, it is equivalent to modify Fourier coefficients $\beta_{n;j,m,l}$ to

$$\beta_{n;j,m,l} - \eta \sum_{j',m',l'\in\mathcal{H}} \alpha_{n;j',m',l'} \beta_{n;j-j',m-m',l-l'}\, \delta t.$$

It follows that:

$$\nabla_{\mathbf{x}} f(\mathbf{x},t_{n+1}) = \nabla_{\mathbf{x}} f(\mathbf{x},t_n) - \eta f(\mathbf{x},t_n)\delta t \nabla_{\mathbf{x}} m(\mathbf{x},t_n) - \eta m(\mathbf{x},t_n)\delta t \nabla_{\mathbf{x}} f(\mathbf{x},t_n). \tag{24}$$

Finally, we summarize the one-step update of Fourier coefficients of ECM density $f$ in Algorithm 2.

**Algorithm 2** One step update of ECM density in SIPF

**Require:** Initial MDE concentration $m_{n-1}$ represented by Fourier coefficients $\alpha_{n-1}$, initial ECM density $f_{n-1}$ represented by Fourier coefficients $\beta_{n-1}$

**for all** $(j, m, l) \in \mathcal{H}$ **do**
  $F_{j,m,l} \leftarrow 0$
  **for all** $(j', m', l') \in \mathcal{H}$ **do**
    $F_{j,m,l} \leftarrow F_{j,m,l} - \eta \alpha_{n-1;j',m',l'} \beta_{n-1;j-j',m-m',l-l'} \delta t$
  **end for**
  $\beta_{n;j,m,l} \leftarrow \beta_{n-1;j,m,l} - F_{j,m,l}$
**end for**

**Ensure:** Update ECM density from input $f_{n-1}$ to $f_n$ via $\beta_n$.

*Updating density of active particles $\rho$.* After updating the ECM density $f$, we can update the density $\rho$. The empirical particle system converging to density $\rho$ reads:

$$dX_p = \gamma \nabla_{\mathbf{x}} f(X_t^p, t)\, dt + \sqrt{2d_n}\, dW_p, \quad p = 1, \ldots, P, \tag{25}$$

where $\sqrt{2d_n}$ is the diffusion coefficient and $W_p$'s are independent standard Brownian motions in $\mathbb{R}^d$.

In the one-step update of density $\rho_n$ represented by particles $\{X_n^p\}_{p=1:P}$, we apply the Euler-Maruyama scheme to solve the SDE (25):

$$X_{n+1}^p = X_n^p + \gamma \nabla_{\mathbf{x}} f(X_n^p, t_n) \cdot \delta t + \sqrt{2d_n \delta t} N_n^p \tag{26}$$

where $N_n^{p\prime}s$ are i.i.d. standard normal distributions with respect to the Brownian paths in the SDE formulation (25).

For $n > 1$, substituting the gradient of the ECM density given by (24) in (26) gives:

$$\begin{aligned} X_{n+1}^p = X_n^p + \gamma \big( & \nabla_{\mathbf{x}} f(\mathbf{x}, t_{n-1}) - \eta \nabla_{\mathbf{x}} f(\mathbf{x}, t_{n-1}) \cdot m(\mathbf{x}, t_{n-1}) \delta t \\ & - \eta \nabla_{\mathbf{x}} m(\mathbf{x}, t_{n-1}) \cdot f(\mathbf{x}, t_{n-1}) \delta t \big) \Big|_{\mathbf{x}=X_n^p} \delta t + \sqrt{2d_n \delta t} N_n^p. \end{aligned} \tag{27}$$

In such particle formulation, the computation of spacial convolution is slightly different from the one in the update of $m$, which is given by (18). Specifically, the spatial convolution is computed as follows:

$$\nabla_{\mathbf{x}} m(\mathbf{x}, t_{n-1}) = -\nabla_{\mathbf{x}} \mathcal{K}_{\delta t} * \left( \frac{m(\mathbf{x}, t_{n-2})}{d_m \cdot \delta t} + \frac{\alpha}{d_m} \cdot \rho(\mathbf{x}, t_{n-1}) \right). \tag{28}$$

In evaluating the convolution $\nabla_{\mathbf{x}} \mathcal{K}_{\delta t} * m_{n-2}(X_n^p)$, we adopt a numerical quadrature scheme to avoid the singularities inherent in $\nabla_{\mathbf{x}} \mathcal{K}_{\delta t}$. Specifically, we compute the integral using quadrature points that are deliberately chosen to avoid the origin, where the singularity may happen. To this end, we denote the standard quadrature points in the domain $\Omega$ as

$$x_{j,m,l} = \left( \frac{jL}{H}, \frac{mL}{H}, \frac{lL}{H} \right),$$

where $j, m, l$ are integers ranging from $-\frac{H}{2}$ to $\frac{H}{2} - 1$.

We compute $\nabla_{\mathbf{x}}\mathcal{K}_{\delta t}$ at positions $\{X_n^p + \overline{X}_n^p - x_{j,m,l}\}_{j,m,l}$, where $\overline{X}_n^p$ is a small spatial shift defined by $\overline{X}_n^p = \frac{H}{2L} + \left\lfloor \frac{X_n^p}{H/L} \right\rfloor \frac{H}{L} - X_n^p$, and $m$ is evaluated at $\{x_{j,m,l} - \overline{X}_n^p\}_{j,m,l}$. We obtain the latter by performing an inverse Fourier transform of the shifted coefficients, where $\alpha_{j,m,l}$ is modified as follows:

$$\alpha_{j,m,l} \exp\left(-i2\pi j \overline{X}_{n;1}^p / L - i2\pi m \overline{X}_{n;2}^p / L - i2\pi l \overline{X}_{n;3}^p / L\right)$$

with $\overline{X}_{n;i}^p$ denoting the $i$-th component of $\overline{X}_n^p$.

Thanks to the particle representation of $\rho(X_n^p, t_{n-1})$ in (10), the term $\nabla_{\mathbf{x}} K_{\delta t} * \rho(X_n^p, t_{n-1})$ is straightforward to compute:

$$\nabla_{\mathbf{x}}\mathcal{K}_{\delta t} * \rho_{n-1}(X_n^p) = \int \mathcal{K}_{\delta t}(X_n^p - y)\rho(y)\, dy \approx \sum_{q=1}^{P} \frac{M}{P} \mathcal{K}_{\delta t}(X_n^p - X_{n-1}^q). \tag{29}$$

We approximate the integral using a sum over $P$ particles, where each particle has mass $M/P$.

Finally, we summarize the one-step update of the Fourier coefficients of the tumor density $\rho$ in Algorithm 3. The whole SIPF method for simulating the cancer cell invasion process within the HAD system is described in Algorithm 4.

**Algorithm 3** One step update of tumor cell density in SIPF

**Data**: Distribution $\rho_n$ represented by empirical samples $X_n$, input MDE concentration $m_{n-1}$ represented by Fourier coefficients $\alpha_{n-1}$, ECM density $f_{n-1}$ represented by Fourier coefficients $\beta_{n-1}$, $\rho_{n-1}$ represented by empirical samples $X_{n-1}$, MDE concentration $m_{n-2}$ represented by Fourier coefficients $\alpha_{n-2}$
**for** $p = 1$ to $P$ **do**
  $X_{n+1}^p \leftarrow X_n^p + \sqrt{2d_n\delta t}N$ ▷ where $N$ is a standard normal distribution
  $\bar{X}_n^p \leftarrow \frac{H}{2L} + \left\lfloor \frac{X_n^p}{H/L} \right\rfloor \frac{H}{L} - X_n^p$
  $\nabla_{\mathbf{x}} f(X_n^p, t_{n-1}) \leftarrow 0$; $f(X_n^p, t_{n-1}) \leftarrow 0$; $m(X_n^p, t_{n-1}) \leftarrow 0$
  **for all** $(j, m, l) \in \mathcal{H}$ **do**
    $F_{j,m,l} \leftarrow \nabla_{\mathbf{x}} \mathcal{K}_{\epsilon,\delta t}(X_n^p + \bar{X}_n^p - x_{j,m,l})$ ▷ $x_{j,m,l} = (jL/H, mL/H, lL/H)$
    $G_{j,m,l} \leftarrow \alpha_{n-2;j,m,l} \exp\left(-2\pi j \bar{X}_{n;1}^p/L - 2\pi m \bar{X}_{n;2}^p/L - 2\pi l \bar{X}_{n;3}^p/L\right)$
    $\nabla_{\mathbf{x}} f(X_n^p, t_{n-1}) \leftarrow \nabla_{\mathbf{x}} f(X_n^p, t_{n-1}) + \frac{i2\pi}{L} \beta_{n-1;j,m,l} e^{i2\pi j X_{n;1}^p/L} e^{i2\pi m X_{n;2}^p/L} e^{i2\pi l X_{n;3}^p/L}$. $(j, m, l)$
    $f(X_n^p, t_{n-1}) \leftarrow f(X_n^p, t_{n-1}) + \beta_{n-1;j,m,l} e^{i2\pi j X_{n;1}^p/L} e^{i2\pi m X_{n;2}^p/L} e^{i2\pi l X_{n;3}^p/L}$
    $m(X_n^p, t_{n-1}) \leftarrow m(X_n^p, t_{n-1}) + \alpha_{n-1;j,m,l} e^{i2\pi j X_{n;1}^p/L} e^{i2\pi m X_{n;2}^p/L} e^{i2\pi l X_{n;3}^p/L}$
  **end for**
  $\hat{G} \leftarrow \text{iFFT}(G)$
  **for** $q = 1$ to $P$ **do**
    $\nabla_{\mathbf{x}} m(X_n^p, t_{n-1}) \leftarrow -\langle F, \hat{G} \rangle \frac{L^3}{H^3} / (d_m \cdot \delta t) - \frac{\alpha M}{d_m P} \mathcal{K}_{\delta t}(X_n^p - X_{n-1}^q)$ ▷ where $\langle \cdot, \cdot \rangle$ denote an inner product corresponding to $L^2(\Omega)$ quadrature
  **end for**
  $\nabla_{\mathbf{x}} f(X_n^p, t_n) \leftarrow \nabla_{\mathbf{x}} f(X_n^p, t_{n-1}) - \eta \nabla_{\mathbf{x}} f(\mathbf{x}, t_{n-1}) \cdot m(\mathbf{x}, t_{n-1}) \delta t - \eta \nabla_{\mathbf{x}} m(\mathbf{x}, t_{n-1}) \cdot f(\mathbf{x}, t_{n-1}) \delta t$
  $X_{n+1}^p \leftarrow X_{n+1}^p + \gamma \cdot \nabla_{\mathbf{x}} f(X_n^p, t_n) \cdot \delta t$
**end for**
**Result**: Output $\rho_{n+1}$ represented by updated $X_{n+1}$.

**Algorithm 4** Stochastic Interacting Particle-Field (SIPF) Method

**Data**: Initial distribution $\rho_0$, initial MDE concentration $m_0$, initial ECM density $f_0$
Generate $P$ i.i.d samples following distribution $\rho_0$, $X_1, X_2, \ldots, X_P$.
**for** $p \leftarrow 1$ to $P$ **do**
  Compute $X_1^p$ by (26), with $f_0$
**end for**
Compute $f_1$ by Algorithm 2 with $f_0$ and $m_0$.
Compute $m_1$ by Algorithm 1 with $m_0$ and $\rho_1 = \sum_{p=1}^P \frac{M}{P} \delta_{X_1^p}$.
**for** step $n \leftarrow 2$ to $N = T/\delta t$ **do**
  Compute $X_n$ by Algorithm 3 with $\rho_{n-1}$, $m_{n-1}$, $\rho_{n-2}$, $m_{n-2}$ and $f_{n-1}$
  Compute $f_n$ by Algorithm 2 with $f_{n-1}$ and $m_{n-1}$.
  Compute $m_n$ by Algorithm 1 with $m_{n-1}$ and $\rho_n = \sum_{p=1}^P \frac{M}{P} \delta_{X_n^p}$.
**end for**

# 3 Numerical Results

To demonstrate the spatio-temporal dynamics of the HAD model for cancer cell invasion, we begin by reproducing a 2D numerical experiment of cancer cell spreading originally presented in [2]. This experiment was derived from the FDM approximation of the system (1). The four snapshots shown in Fig. 1 illustrate the temporal progression of the tumor cell density distribution, with the first sub-figure representing the initial conditions. Specifically, the initial data is given by:

$$\rho(x, y, 0) = e^{-r^2/\epsilon}, \quad r^2 = x^2 + y^2, \quad r \in [0, 0.1], \tag{30}$$

$$f(x, y, 0) = 1 - 0.5\rho(x, y, 0), \tag{31}$$

$$m(x, y, 0) = 0.5\,\rho(x, y, 0), \tag{32}$$

where we use the same parameters as in [2] for the system (1):

$$d_n = d_m = 0.001, \quad \gamma = 0.005, \quad \eta = 10, \quad \alpha = 0.1, \quad \beta = 0, \quad \epsilon = 0.0025. \tag{33}$$

The tumor cell equation (1) does not include terms for cell birth and death, and the zero flux boundary conditions ensure that the total number of cells remains constant. This conservation property allows us to verify the accuracy of the FDM. To measure the deviation from the expected conservation, we define the error at time $t = T$ as follows:

$$\text{Error}_{t=T} = \frac{\sum_i(\rho_{i,t=T}) - \sum_i(\rho_{i,t=0})}{\sum_i(\rho_{i,t=0})}, \tag{34}$$

where $\rho_i$ refers to the density of the cell within the $i$-th grid of FDM. It has demonstrated an accuracy within 0.01%, indicating high reliability in the numerical simulation. We observe that the main body of the tumor invades slowly. At the forefront, a high-density cell zone emerges, which subsequently detaches to form an independent circular cluster of cells that penetrates deeper into the ECM.

All the experiments presented in this work were carried out on the HPC2021 system at the University of Hong Kong, which is equipped with 16-core Intel Xeon 6226R processors and an NVIDIA Tesla V100 32GB SXM2 GPU.

## 3.1 Comparing radial/FDM/SIPF methods in 3D

In this subsection, we aim to generalize the model to a 3D spatial domain, which allows for a more detailed exploration of the spatio-temporal evolution of the system. To achieve this, we set the initial conditions as follows:

$$\begin{aligned} \rho(x, y, z, 0) &= e^{-r^2/\epsilon}, \quad r^2 = x^2 + y^2 + z^2, \quad r \in [0, 0.1], \\ f(x, y, z, 0) &= 1 - 0.5\,\rho(x, y, z, 0), \\ m(x, y, z, 0) &= 0.5\,\rho(x, y, z, 0). \end{aligned} \tag{35}$$

Unless otherwise stated, the parameter values used in the subsequent simulations were the same as those employed in the previous 2D experiments, as given by (33). In

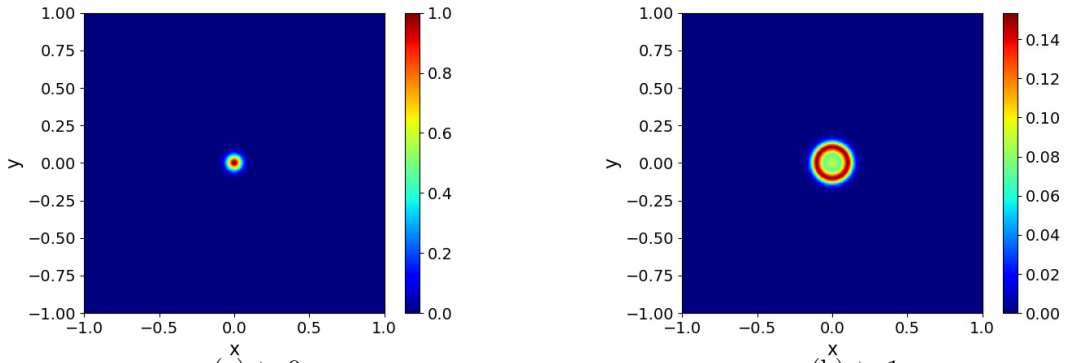


(a) t=0 (b) t=1

(c) t=2 (d) t=4

Figure 1: A numerical simulation of the system (1), with constant tumor cell diffusion, reveals the spatio-temporal dynamics of the tumor invasion process. The figure shows the emergence of a ring of cells that breaks away from the primary tumor mass and invades deeper into the ECM.

the radially symmetric case, we can denote the cancer cell invasion HAD system (1) as $\rho(x,y,z,t) = \rho(r,t)$, $f(x,y,z,t) = f(r,t)$, and $m(x,y,z,t) = m(r,t)$. This allows us to study the system's behavior in a simplified form and gain insights into the spatio-temporal dynamics of the tumor invasion process.

$$\begin{cases} \rho_t = d_n \left( \dfrac{\partial^2 \rho}{\partial r^2} + \dfrac{2}{r} \dfrac{\partial \rho}{\partial r} \right) - \gamma \left( \dfrac{\partial \rho}{\partial r} \dfrac{\partial f}{\partial r} + \rho \cdot \left( \dfrac{\partial^2 f}{\partial r^2} + \dfrac{2}{r} \dfrac{\partial f}{\partial r} \right) \right), \\ f_t = -\eta m f, \\ m_t = d_m \left( \dfrac{\partial^2 m}{\partial r^2} + \dfrac{2}{r} \dfrac{\partial m}{\partial r} \right) - \beta m + \alpha \rho. \end{cases} \tag{36}$$

To ensure accuracy in our numerical experiments, we use a very fine mesh to compute the radial solution, which serves as the reference solution. We then compare the FDM and SIPF methods with the radial solutions in this experiment. For the FDM simulations, we use a uniform mesh with $\delta x = \delta y = \delta z = 1/101$ and a time step $\delta t = 10^{-2}$. For the radial 1D simulations, we use a uniform mesh with $\delta r = 1/301$ and a time step $\delta t = 10^{-3}$. For the SIPF method, we discretize the MDE concentration $m$ using $H = 24$ Fourier basis in each spatial dimension and approximate the distribution $\rho$ with $P = 10,000$ particles. We then simulate the evolution of $m, f$ and $\rho$ using Algorithm 4 with a time step $\delta t = 10^{-2}$.

Fig.2 presents 1D slices of the results from the FDM and SIPF methods, depicting the temporal progression of tumor cell invasion into the host tissue. These results indicate that the SIPF method performs with higher accuracy than the FDM method, particularly at peak values.

To further demonstrate the accuracy and convergence rate of the FDM and SIPF methods, we provide three tables (Tables 1-3) that compare the relative $L^2$ error of $m$ obtained from these methods with the reference solution. The reference solution is computed by the proposed radial case on a uniform mesh with $\delta r = 1/801$ and $\delta t = 10^{-3}$. To compare the SIPF method with the radial reference solution, we convert 3D spatial domain data to a 1D radial representation and compare it with the reference radial solution. The spatial domain data, denoted as $M$, is derived from the frequency domain data, which are the Fourier coefficients represented by $\tilde{M}_\alpha$. Specifically, $M$ is obtained by taking the real part of the result from the Inverse Fast Fourier Transform (IFFT) applied to $\tilde{M}_\alpha$. We define $n$ bins with edges $r_i$ for $i = 0$ to $n$. The relative $L^2$ error between the SIPF mean and the reference radial solution is defined as:

$$\text{Relative } L^2 \text{ Error} = \frac{\sqrt{\sum_i (M_i - R_i)^2}}{\sqrt{\sum_i (R_i)^2}}, \tag{37}$$

where $M_i$ represents the SIPF mean in the $i$-th bin, and $R_i$ denotes the radial reference value in the same bin.

In Table 1, the rate of convergence, denoted as *Rate*, is computed using the following formula:

$$\text{Rate} = \left| \frac{\log(\epsilon_{\text{prev}}/\epsilon_{\text{curr}})}{\log(\delta x_{\text{prev}}/\delta x_{\text{curr}})} \right|, \tag{38}$$

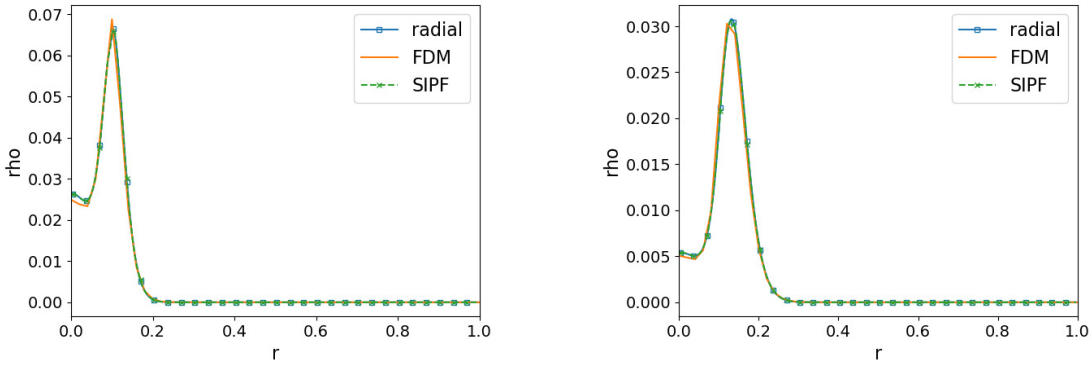


(a) t=1




(b) t=2

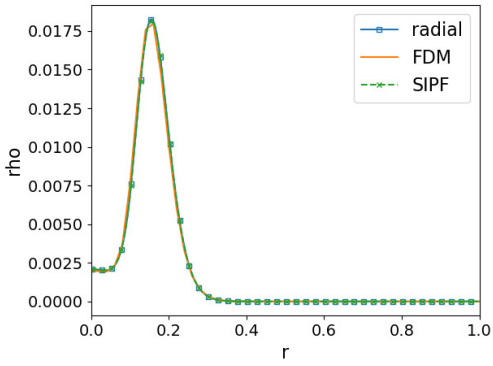


(c) t=3

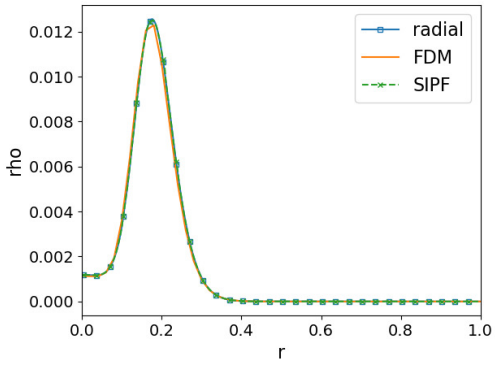


(d) t=4

Figure 2: 3D numerical solutions of the system (1) with constant tumor cell diffusion showing the cell density computed by radial, FDM, and SIPF.

where $\epsilon_{\text{prev}}$ and $\epsilon_{\text{curr}}$ are the relative $L^2$ errors at the previous and current grid sizes, respectively, while $\delta x_{\text{prev}}$ and $\delta x_{\text{curr}}$ are the spatial step sizes at the previous and current grid sizes, respectively.

Similarly, we can define the ratio in this way. As shown in Table 1, the FDM method not only yields inaccurate results but also requires significant computational time. As the grid size increases, the computational runtime of FDM escalates significantly. However, the accuracy of the numerical method does not improve proportionally with the finer grid, failing to justify the substantial increase in runtime. Conversely, Table 2 demonstrates the variations in computational runtime and relative $L^2$ error as the time step $\delta t$ changes for the SIPF method. Unlike FDM, SIPF is less computationally intensive, and larger $\delta t$ values still maintain commendable accuracy. Additionally, Table 3 shows that increasing the number of particles significantly impacts the runtime.

Fig.3 shows the relative $L^2$ error of the MDE concentration $m$ at the final time $T = 4$ for different time steps $\delta t$, particle numbers $P$, and Fourier modes $H$. By fitting the slope of the error versus $\delta t$ in logarithmic scale, we observe that $e(\delta t) = \mathcal{O}(\delta t^{1.0130})$, indicating that the algorithm is approximately first-order in time. Additionally, by fitting the slope of the error versus $P$ in the logarithmic scale, we find that $e(P) = \mathcal{O}(P^{-0.5587})$. To provide a clearer picture of the convergence of the MDE concentration $m$ versus Fourier mode $H$, we plot the errors in semi-log scale in Fig.3(c), which indicates an exponential convergence rate $\mathcal{O}(e^{-0.1608H})$. As the number of Fourier modes increases, there is a clear improvement in accuracy, measured by the relative $L^2$ error. Experiments indicate that when we set particle number $P$ to be 10,000, time step $\delta t$ to be 0.01, and Fourier mode $H$ to be 24, there is a good trade-off between accuracy and computational time. The following SIPF algorithm adopts this configuration with no specific mention.

| FDM Grid | Run time(s) | Ratio | Relative $L^2$ Error | Rate |
|---|---|---|---|---|
| $21 \times 21 \times 21$ | 15.54 | | 1.1430 | |
| $41 \times 41 \times 41$ | 132.87 | 3.09 | 0.2808 | 2.02 |
| $61 \times 61 \times 61$ | 465.08 | 3.09 | 0.1253 | 1.99 |
| $81 \times 81 \times 81$ | 1126.01 | 3.07 | 0.0694 | 2.05 |
| $101 \times 101 \times 101$ | 2238.85 | 3.08 | 0.0447 | 2.01 |

Table 1: 3D run time and relative $L^2$ error of FDM vs. grid size (at $\delta t = 0.01$).

## 3.2 Regime of Small Diffusion Coefficient

In this subsection, we change the diffusion coefficient $d_n$, while keeping all other conditions and parameters unchanged. As $d_n$ decreases, the FDM becomes more computationally expensive. In Fig.4, we set $d_n = 0.0002$. Compared with Fig.2, we can see the simulation results in Fig.4 are not good. As the diffusion coefficient $d_n$ decreases, the peak of tumor density becomes steeper, leading to instability in the FDM method. This instability requires a very fine discretization to accurately resolve the peak, which

| dt(s) | Run time(s) | Ratio | Relative $L^2$ Error | Rate |
|---|---|---|---|---|
| 0.1 | 10.37 | | 9.12E-02 | |
| 0.05 | 18.06 | 0.80 | 4.50E-02 | 1.02 |
| 0.01 | 66.98 | 0.81 | 8.78E-03 | 1.02 |
| 0.005 | 117.42 | 0.81 | 4.36E-03 | 1.01 |
| 0.001 | 413.01 | 0.79 | 8.59E-04 | 1.01 |

Table 2: 3D run time and relative $L^2$ error of SIPF vs. $\delta t$ (at $P = 10000$).

| Particle Numbers | Run time(s) | Ratio | Relative $L^2$ error | Rate |
|---|---|---|---|---|
| 5000 | 29.70 | | 1.34E-02 | |
| 10000 | 66.98 | 0.95 | 8.78E-03 | 0.61 |
| 20000 | 358.44 | 2.42 | 5.89E-03 | 0.58 |
| 30000 | 1129.15 | 2.83 | 4.77E-03 | 0.52 |
| 40000 | 1995.86 | 1.98 | 4.11E-03 | 0.51 |

Table 3: 3D run time and relative $L^2$ error of SIPF vs. $P$ (at $\delta t = 0.01$).

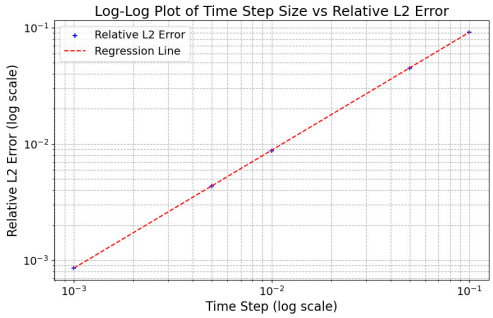


(a) vs. time step $\delta t$ on log-scale

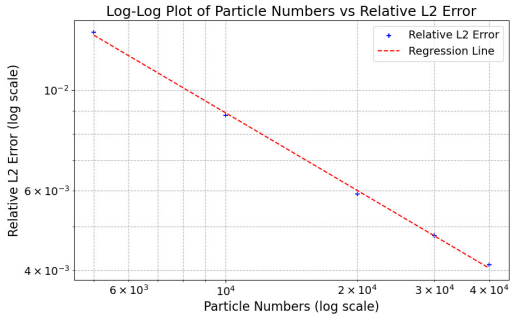


(b) vs. particle number $P$ on log-scale

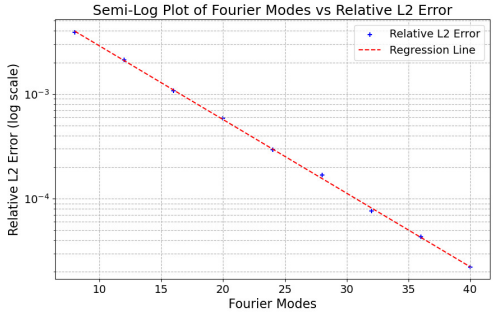


(c) vs. Fourier mode $H$ on semi-log-scale

Figure 3: 3D relative $L^2$ errors of $m$ in SIPF (radial solution being the reference).

in turn leads to a substantial increase in computational time. On the other hand, the SIPF method remains stable and accurate even under these conditions.

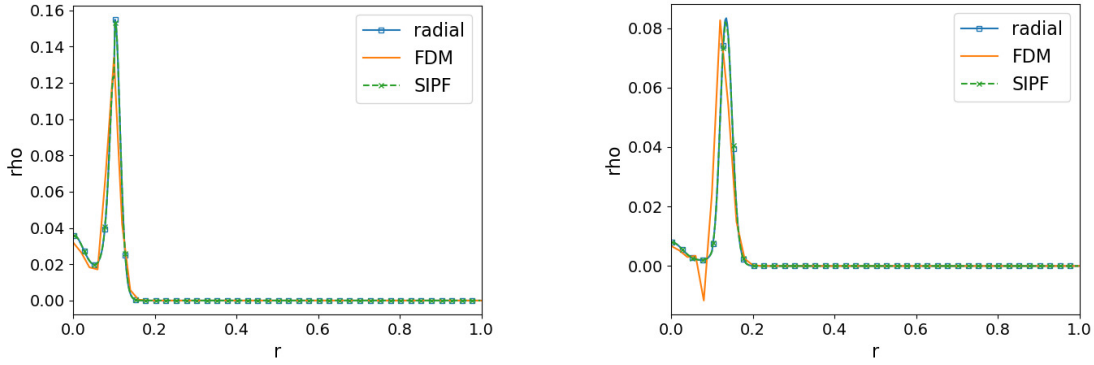


(a) t=1




(b) t=2

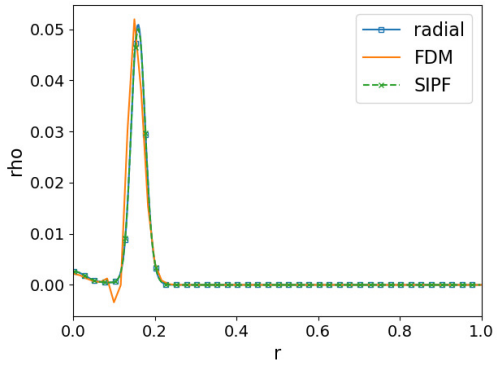


(c) t=3

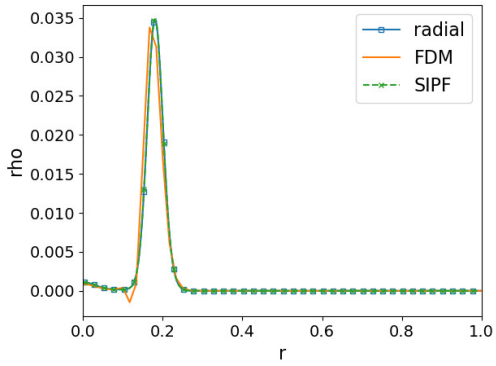


(d) t=4

Figure 4: Comparing radial solutions, FDM (red) and SIPF (green) at $d_n = 0.0002$, shows under-shoot (violating positivity) and inaccurate peak locations in FDM.

## 3.3 Two Clusters of Cancer Cells Evolution

All of the experiments conducted so far have satisfied the initial data symmetry. In this subsection, we explore the behavior of the SIPF algorithm when dealing with non-radial initial data. Our simulations demonstrate that the SIPF algorithm is equally effective in asymmetric situations. Specifically, we present a 3D SIPF simulation of cancer cells spreading dynamics from two clusters of cells with non-radial initial conditions. The initial condition is as follows:

$$\rho_1(x,y,z,0) = e^{-r_1^2/\epsilon}, \quad r_1^2 = (x-a)^2 + (y-b)^2 + (z-c)^2, \quad r \in [0, 0.1] \tag{39}$$

$$\rho_2(x,y,z,0) = e^{-r_2^2/\epsilon}, \quad r_2^2 = (x-d)^2 + (y-e)^2 + (z-f)^2, \quad r \in [0, 0.1] \tag{40}$$

$$\rho(x,y,z,0) = \rho_1(x,y,z,0) + \rho_2(x,y,z,0). \tag{41}$$

Here we set $a = b = c = 0.1, d = e = f = -0.1$ as the parameters for the initial condition, and present the fusion/spreading process of the two clusters in Fig.5. As

shown in Fig.5, the two clusters of cells diffuse outward over time, intersect, and then merge, continuing their invasion outward. Notably, in the absence of any specified interactions between the two clusters of cells, the diffusion process remains similar to that of a single cluster of cells.

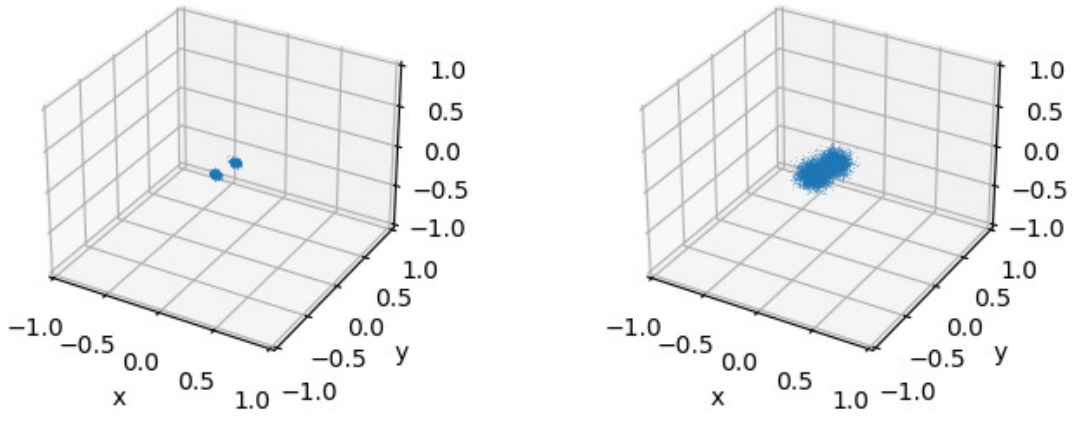


(a) t=0




(b) t=0.3

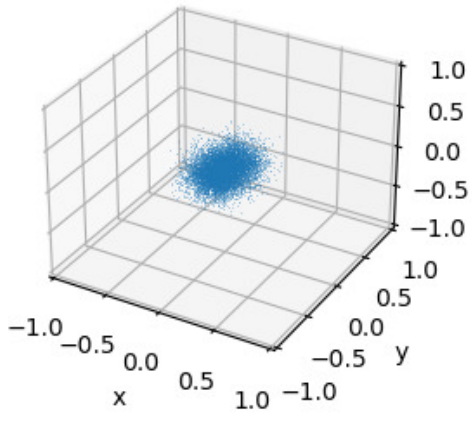


(c) t=0.7

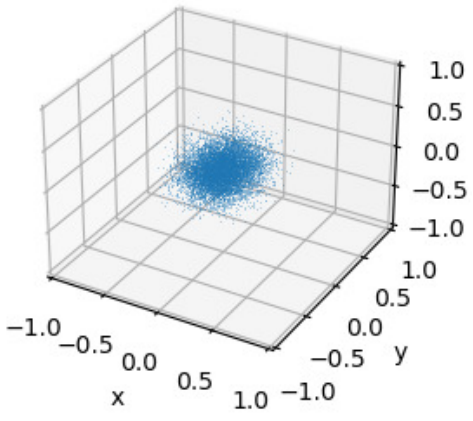


(d) t=1

Figure 5: Two clusters of cancer cells merge into a larger single cluster and spread further.

## 3.4 Comparing FDM and SIPF based on Integral Identities

In Section 3.1, we consider the initial condition (35), which satisfies the following relation:

$$\int_\Omega m(X,0)\,dX = 2\pi \int_0^{0.1} e^{-\frac{r^2}{\epsilon}} r^2\,dr = \frac{1}{2}\int_\Omega \rho(X,0)\,dX,\ \beta = 0,$$

as shown in (6). We also have the following relationship, which holds for all $t \geq 0$:

$$\int_\Omega m(X,t) = 4\pi\alpha t \int_0^{0.1} e^{-\frac{r^2}{\epsilon}} r^2\, dr + 2\pi \int_0^{0.1} e^{-\frac{r^2}{\epsilon}} r^2\, dr. \tag{42}$$

We evaluate the integral $\int_\Omega m(X,t)$ using the radial solution, FDM, and SIPF methods, and compare the results with the reference value in (42). By using Eq.(9), Eq.(42) and the condition

$$\int_\Omega \ln f_0\, dX = 4\pi \int_0^{0.1} \ln\left(1 - 0.5e^{-r^2/\epsilon}\right) r^2\, dr,$$

we can show that $f$ satisfies the following relation:

$$\begin{aligned}\int_\Omega \ln f(X,t) = 4\pi &\int_0^{0.1} \ln\left(1 - 0.5e^{-r^2/\epsilon}\right) r^2\, dr \\ &- \eta\left(2\pi\alpha t^2 \int_0^{0.1} e^{-\frac{r^2}{\epsilon}} r^2\, dr + 2\pi t \int_0^{0.1} e^{-\frac{r^2}{\epsilon}} r^2\, dr\right).\end{aligned} \tag{43}$$

To compare the accuracy of the SIPF, radial, and FDM methods in approximating the solution $m(X,T)$, we define the reference value of $m$, denoted as $m_r$, which is the integral of $m(X,T)$ over the domain $\Omega$ as given in Eq.(42). For the SIPF method, we compute $m$ at time $T$ as $m^{\text{SIPF}} = \alpha_{T;0,0,0} \cdot L^3$, where $\alpha$ is a Fourier coefficient defined previously (see Eq.(11)), and $L$ is a characteristic length scale. In the radial method, we discretize the radial coordinate $r$ into bins with widths $\delta r$ (the radial step size), and values of $m$ corresponding to these discrete radii. The integral of $m$ at time $T$ is approximated as a sum: $m^{\text{radial}} = \sum_i (m_{i,t=T}) \cdot 4\pi r_i^2 \cdot \delta r$, where $m_i$ is the value of $m$ at the $i$-th radial position, and $r_i$ is the radius at the $i$-th position. For the FDM, we compute $m$ at time $T$ as $m^{\text{FDM}} = \sum_j (m_{j,t=T}) \cdot (\delta x)^3$, where $\delta x$ is the spatial step size used in the FDM.

To quantify the accuracy of the different methods, we define the relative $L^2$ error of $m$ at time $T$, denoted as $Error_m$, as follows:

$$\text{Error}_\text{m} = \frac{|m_n - m_r|}{|m_r|}, \tag{44}$$

where $m_n$ represents any of the numerically computed values from the SIPF, radial, or FDM. Similarly, we can define the relative error of $\ln f$ using a similar equation.

The relative error of $m$ and $\ln f$ at different times is shown in Fig.6. The SIPF method consistently demonstrates better performance compared to the FDM method. At the final time, the relative error of both $m$ and $\ln f$ is approximately an order of magnitude lower for the SIPF method compared to the FDM method. Overall, the SIPF method outperforms the FDM method in terms of accuracy.

# 4 Conclusion and Future Work

In this paper, we have developed the SIPF algorithm and demonstrated its efficacy and accuracy in computing cancer cell invasion within the HAD system. The SIPF algorithm

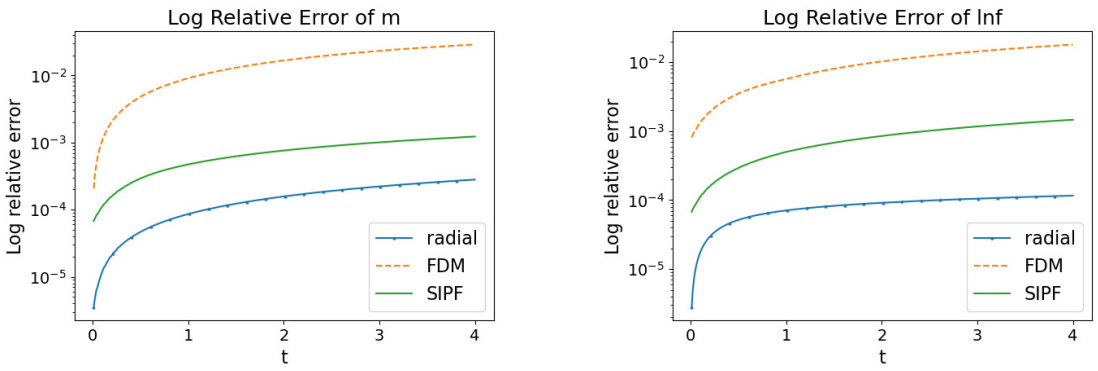


(a) $m$ (b) $\ln f$

Figure 6: Relative error comparison in computing the integrals of Eqs.(42)(43) by radial solution (blue), FDM (red), and SIPF (green).

is recursive with no history dependence and we approximate the cell density by empirical measures of particles and approximate the coupled field variables (MDEs and ECM) by the spectral method. Because the field variables (concentration) are smoother than the cell density, the spectral method works well with only a few dozen Fourier modes. The spreading behavior of the cell density is resolved by $10,000$ particles. Our results show that the FDM is both time-consuming and inaccurate in 3D computations of tumor invasion. Moreover, the SIPF algorithm can simulate complex multi-modal cell development, such as multiple cancer cell spreading and merging dynamics. Therefore, the SIPF method offers a promising alternative for accurately modeling and simulating complex biological systems.

In future works, we will conduct a deep particle study [26, 27] based on the data generated from the SIPF simulations presented in this paper. We aim to explore more complex models of tumor invasion to better capture the growth dynamics. Specifically, we plan to incorporate oxygen supply into the existing system to enable more precise computations [1]. In addition, the coupled two-species cancer invasion haptotaxis model has practical significance in real-world applications and in understanding realistic tumor progression [5]. While we have briefly discussed a non-radial 3D case study in this paper, there is still much to explore in this area, and we plan to further investigate this topic in future research.

# Acknowledgements

ZW was partially supported by NTU SUG-023162-00001. JX by NSF grant DMS-2309520. ZZ was supported by the National Natural Science Foundation of China (Project 12171406), the Hong Kong RGC grant (Projects 17307921 and 17304324), the Outstanding Young Researcher Award of HKU (2020-21), Seed Funding for Strategic Interdisciplinary Research Scheme 2021/22 (HKU), and Seed Funding from the HKU-TCL Joint Research Centre for Artificial Intelligence.

# References


[1] A. Anderson and M. Chaplain. "Continuous and Discrete Mathematical Models of Tumor-induced Angiogenesis". In: *Bulletin of Mathematical Biology* 60.5 (1998), pp. 857–899.

[2] A. R. Anderson, M. A. Chaplain, E. L. Newman, R. J. Steele, and A. M. Thompson. "Mathematical modelling of tumour invasion and metastasis". In: *Computational and mathematical methods in medicine* 2 (2000), pp. 129–154.

[3] S. Bekisz and L. Geris. "Cancer modeling: From mechanistic to data-driven approaches, and from fundamental insights to clinical applications". In: *Journal of Computational Science* 46 (2020), p. 101198.

[4] M. Chaplain. "Avascular growth, angiogenesis and vascular growth in solid tumours: The mathematical modelling of the stages of tumour development". In: *Mathematical and computer modelling* 23.6 (1996), pp. 47–87.

[5] F. Dai and L. Ma. "Boundedness in a two-dimensional two-species cancer invasion haptotaxis model without cell proliferation". In: *Zeitschrift für angewandte Mathematik und Physik* 74.2 (2023), p. 54.

[6] I. Fatkullin. "A study of blow-ups in the Keller–Segel model of chemotaxis". In: *Nonlinearity* 26.1 (2012), p. 81.

[7] P. Gopika, N. Ranwan, and N. Chamakuri. "Residual-Based a Posteriori Error Estimator for a Multi-scale Cancer Invasion Model." In: *CoRR* (2023).

[8] T. Y. Hou and R. Li. "Computing nearly singular solutions using pseudo-spectral methods". In: *Journal of Computational Physics* 226.1 (2007), pp. 379–397.

[9] A. M. Jarrett, E. A. Lima, D. A. Hormuth, M. T. McKenna, X. Feng, D. A. Ekrut, A. C. M. Resende, A. Brock, and T. E. Yankeelov. "Mathematical models of tumor cell proliferation: A review of the literature". In: *Expert review of anticancer therapy* 18.12 (2018), pp. 1271–1286.

[10] D. Katsaounis, M. A. Chaplain, and N. Sfakianakis. "Stochastic differential equation modelling of cancer cell migration and tissue invasion". In: *Journal of Mathematical Biology* 87.1 (2023), p. 8.

[11] G. Liţcanu and C. Morales-Rodrigo. "Asymptotic behavior of global solutions to a model of cell invasion". In: *Mathematical Models and Methods in Applied Sciences* 20.09 (2010), pp. 1721–1758.

[12] J.-G. Liu and R. Yang. "A random particle blob method for the Keller-Segel equation and convergence analysis". In: *Math. Comput.* 86.304 (2017), pp. 725–745.

[13] J.-G. Liu and R. Yang. "Propagation of chaos for the Keller–Segel equation with a logarithmic cut-off". In: *Methods Appl. Analysis* 26.4 (2019), pp. 319–348.

[14] G. Luo and T. Y. Hou. "Toward the finite-time blowup of the 3D axisymmetric Euler equations: a numerical investigation". In: *Multiscale Modeling & Simulation* 12.4 (2014), pp. 1722–1776.

[15] A. Marciniak-Czochra and M. Ptashnyk. "Boundedness of solutions of a haptotaxis model". In: *Math Models Methods Applied Sci* 20.03 (2010), pp. 449–476.

[16] S. Mischler and C. Mouhot. "Kac's program in kinetic theory". In: *Inventiones mathematicae* 193 (2013), pp. 1–147.

[17] I. Ramis-Conde, M. A. Chaplain, and A. R. Anderson. "Mathematical modelling of cancer cell invasion of tissue". In: *Mathematical and Computer Modelling* 47.5 (2008). Towards a Mathematical Description of Cancer: Analytical, Numerical and Modelling Aspects, pp. 533–545.

[18] M. Retsky, D. Swartzendruber, R. H. Wardwell, and P. D. Bame. "Is Gompertzian or exponential kinetics a valid description of individual human cancer growth?" In: *Medical hypotheses* 33.2 (1990), pp. 95–106.

[19] R. L. Siegel, A. N. Giaquinto, and A. Jemal. "Cancer statistics, 2024." In: *CA: a cancer journal for clinicians* 74.1 (2024).

[20] J. Smolle and H. Stettner. "Computer simulation of tumour cell invasion by a stochastic growth model". In: *Journal of Theoretical Biology* 160.1 (1993), pp. 63–72.

[21] A. Stevens. "A stochastic cellular automaton modeling gliding and aggregation of myxobacteria". In: *SIAM Journal on Applied Mathematics* 61.1 (2000), pp. 172–182.

[22] A. Stevens. "The derivation of chemotaxis equations as limit dynamics of moderately interacting stochastic many-particle systems". In: *SIAM Journal on Applied Mathematics* 61.1 (2000), pp. 183–212.

[23] A. Stevens and H. G. Othmer. "Aggregation, blowup, and collapse: the ABC's of taxis in reinforced random walks". In: *SIAM Journal on Applied Mathematics* 57.4 (1997), pp. 1044–1081.

[24] Y. Tao and G. Zhu. "Global solution to a model of tumor invasion". In: *Appl. Math. Sci* 1.48 (2007), pp. 2385–2398.

[25] P. Veeresha, E. Ilhan, D. Prakasha, H. M. Baskonus, and W. Gao. "Regarding on the Fractional Mathematical Model of Tumour Invasion and Metastasis." In: *CMES-Computer Modeling in Engineering & Sciences* 127.3 (2021).

[26] Z. Wang, J. Xin, and Z. Zhang. "DeepParticle: learning invariant measure by a deep neural network minimizing Wasserstein distance on data generated by an interacting particle method". In: *J. Computational Physics* 464 (2022), p. 111309.

[27] Z. Wang, J. Xin, and Z. Zhang. "A DeepParticle method for learning and generating aggregation patterns in multi-dimensional Keller–Segel chemotaxis systems". In: *Physica D: Nonlinear Phenomena* (2024), p. 134082.

[28] Z. Wang, J. Xin, and Z. Zhang. "A Novel Stochastic Interacting Particle-Field Algorithm for 3D Parabolic-Parabolic Keller-Segel Chemotaxis System". In: *arXiv preprint arXiv:2309.13554* (2023).